

Influence of Solid-State Packing of Dipolar Merocyanine Dyes on Transistor and Solar Cell Performances

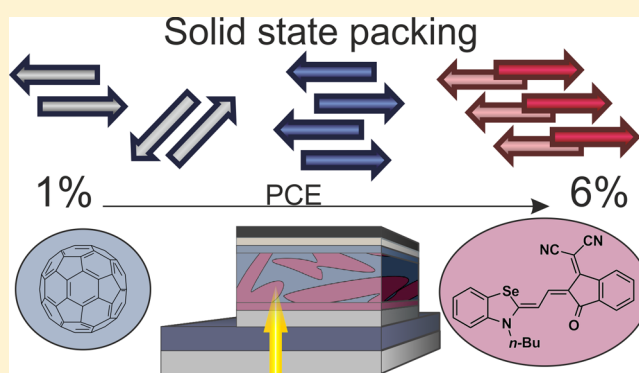
Alhama Arjona-Esteban,[†] Julian Krumrain,[‡] Andreas Liess,[†] Matthias Stolte,[†] Lizhen Huang,[†] David Schmidt,[†] Vladimir Stepanenko,[†] Marcel Gsänger,[†] Dirk Hertel,[‡] Klaus Meerholz,^{*,‡} and Frank Würthner^{*,†}

[†]Institut für Organische Chemie & Center for Nanosystems Chemistry, Universität Würzburg, Am Hubland, 97074 Würzburg, Germany

[‡]Department Chemie, Universität zu Köln, Luxemburgerstr. 116, 50939 Köln, Germany

Supporting Information

ABSTRACT: A series of nine dipolar merocyanine dyes has been studied as organic semiconductors in transistors and solar cells. These dyes exhibited single-crystal packing motifs with different dimensional ordering, which can be correlated to the performance of the studied devices. Hereby, the long-range ordering of the dyes in staircase-like slipped stacks with *J*-type excitonic coupling favors charge transport and improves solar cell performance. The different morphologies of transistor thin films and solar cell active layers were investigated by UV-vis, AFM, and XRD experiments. Selenium-containing donor-acceptor (D-A) dimethine dye **4** showed the highest hole mobility of 0.08 cm² V⁻¹ s⁻¹. BHJ solar cells based on dye **4** were optimized by taking advantage of the high crystallinity of the donor material and afforded a PCE of up to 6.2%.



INTRODUCTION

Since the first planar heterojunction (PHJ) organic solar cell with around 1% power conversion efficiency (PCE) was reported by Tang in 1986,¹ much progress has been achieved in the field of organic photovoltaics (OPV). Thus, a plethora of bulk heterojunction (BHJ) solar cells processed both from solution and by sublimation, based either on polymers or small molecules, have been reported since then with efficiencies approaching 10%.^{2–9} This progress indeed raises expectations for commercialization because organic materials offer the advantages of low-cost production and flexibility in molecular design as well as several applications not accessible for silicon-based solar cells, such as transparent devices for covering windows or flexible solar cells attached to textiles for charging mobile devices.

Among the various kinds of molecules used so far as the donor counterpart to the ubiquitously utilized fullerene acceptors in BHJ active layers, an increasing number of molecules with alternating electron donor (D) and acceptor (A) subunits have been reported in recent years.^{10–12} These materials have the advantages of a low band gap and high tinctorial strength, with absorption properties that are tunable by carefully designing the corresponding donor and acceptor units. The common approach is based on D–A–D and A–D–A scaffolds for small molecules or (D–A)_n structures for polymers to avoid a broadening of the density of states by

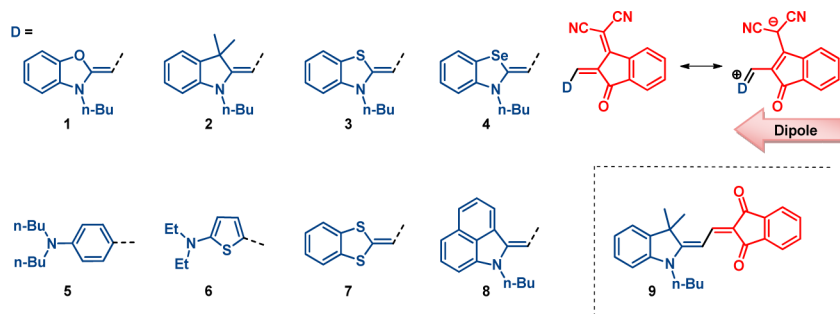
dipolar disorder, which is considered to be detrimental for charge transport according to the Gaussian disorder model (GDM).¹³ As a consequence, dipolar dyes (D–A dyes, push–pull dyes) such as merocyanines have been omitted throughout the entire field of organic electronics during the last three decades, including organic photovoltaics. However, dipolar disorder arises only for randomly distributed dipolar molecules. The fact that these molecules tend to pack tightly in antiparallel dimers with no overall dipole moment accordingly opens the door to applications in organic photovoltaics.¹⁴ Indeed, in 2008, our groups already reported the first merocyanine-based solar cell, which showed a respectable PCE of 1.7%.¹⁵ Later, we confirmed our concept with improved materials for both solution- (HB366, 4.5%)¹⁶ as well as vacuum-processed devices (HB194, 5.8%).¹⁷ The groups of Blanchard, Roncali, and Wong, among others,^{18–24} have investigated other types of D–A dyes and pushed solar cell devices based on dipolar D–A molecules even further, reaching PCEs of up to 6.8%.²⁵

Still, despite the continuously increasing performance of organic solar cells, it is difficult to predict the success of a given absorber molecule because the PCE depends on many parameters beyond those given by the individual molecule. For this reason, many studies, including our previous ones on

Received: June 29, 2015

Published: September 28, 2015

Chart 1. Chemical and Resonance Structures of Merocyanine Dyes Investigated in This Work Bearing Acceptor Units 2-(3-Oxo-2,3-dihydro-1H-inden-1-ylidene)malononitrile (1–8) and 1,3-Indanedione (9)



D–A dye-based OPV, focus their attention on a particularly outstanding molecule and avoid rationalizing the failure of structurally similar ones.

In this article, we report, for the first time, a comprehensive investigation of a series of structurally related D–A dyes, i.e., a series of nine merocyanine dyes (Chart 1) bearing the same 2-(3-oxo-2,3-dihydro-1H-inden-1-ylidene)malononitrile acceptor moiety, that exhibit similar optical absorption properties yet show very different performances in organic solar cells (OSC) and organic thin-film transistor (OTFT) devices. With the help of UV–vis spectroscopy, atomic force microscopy (AFM), and X-ray diffraction (XRD) measurements of thin films and single-crystal analyses, the variations in their performances are attributed to different packing arrangements of the dyes in the solid state. Consequently, we correlate the supramolecular packing of merocyanines with both OTFT and OSC performances.

RESULTS

Synthesis. Dyes depicted in Chart 1 were obtained by Knoevenagel condensation between an aldehyde or imine derivative and the C–H active acceptor unit in acetic anhydride in moderate to good yields. Dyes 2, 5, and 9 have been described previously.^{26–28} The synthetic procedures of all new dyes can be found in the Supporting Information.

Molecular Properties. The optical properties of the dyes described in Chart 1 were investigated by means of UV–vis and electro-optical absorption (EOA) spectroscopy. In addition, cyclic voltammetry (CV) was performed to estimate the frontier molecular orbital (FMO) energy levels. The optical absorption spectra and the estimated FMO levels are represented in Figure 1, and the corresponding data are listed in Table 1. All UV–vis, EOA, and CV spectra of the reported dyes can be found in Figures S1–S8.

The optical properties are similar for dyes 2–7 containing 2-(3-oxo-2,3-dihydro-1H-inden-1-ylidene)malononitrile as the acceptor moiety, featuring absorption maxima around 580 nm and extinction coefficients (ϵ_{\max}) of about $52\text{--}70 \times 10^3 \text{ M}^{-1} \text{ cm}^{-1}$. The tinctorial strength ($\mu_{\text{eg}}^2 \text{ M}^{-1}$) remains strong in all cases ($0.20\text{--}0.26 \text{ D}^2 \text{ mol g}^{-1}$). X-ray photoelectron spectroscopy (XPS) studies on merocyanines bearing azaheterocyclic donor units containing oxygen, sulfur, and selenium have analyzed the conjugation and partial charge distribution over the heteroatom within the donor unit.²⁹ The heteroatom's positive charge contribution and conjugation were found to decrease in the order $\text{O} > \text{S} > \text{Se}$. These studies concluded that the positive charge (zwitterionic structure) in the donor moiety of the merocyanines mainly lies on the nitrogen atom, except

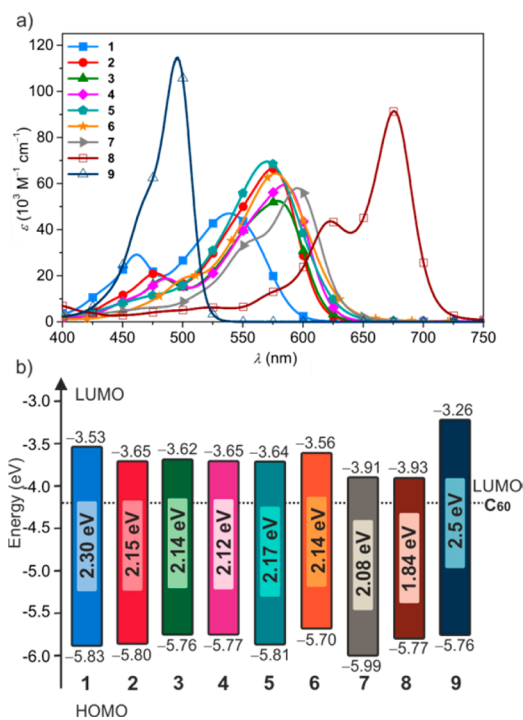


Figure 1. (a) UV–vis spectra of dyes 1 (blue squares), 2 (red circles), 3 (green triangles), 4 (pink rhombi), 5 (cyan pentagones), 6 (orange stars), 7 (gray triangles), 8 (brown open squares), and 9 (dark blue open triangles) at 10^{-5} M in CH_2Cl_2 , 298 K. (b) Schematic representation of the HOMO and LUMO levels of dyes 1–9 and their positions relative to the LUMO level of the most commonly used fullerene acceptor material, C_{60} , calculated from CV measurements (Fc/Fc^+ value of -5.15 eV^{35} vs vacuum) and the optical gap from the UV–vis absorption maxima, respectively.

for the benzoxazole heterocycle, where the contribution of the O^+ form is no longer negligible.^{30,31} This conjugation effect can be observed in the absorption spectrum of dye 1, which is slightly blue-shifted in comparison with that of the other dyes of this series, in particular, dyes 3 and 4, similar to other benzoxazole-containing compounds described in the literature.³² Dyes bearing a benzo[*c,d*]indole donor moiety have been found to show the highest effective conjugation length among nitrogen-containing heterocycles,^{33,34} thus shifting the molecular absorption to the near-infrared region, as seen for dye 8. On the other hand, dye 9 shows a sharper absorption at shorter wavelengths due to the lack of the dicyanovinyl acceptor group, i.e., the shorter conjugation path provided by the 1,3-indanedione acceptor unit.

Table 1. Optical, Dipolar, and Electrochemical Properties of Compounds 1–9 Extracted from UV–Vis,^a EOA,^b and CV^c Measurements

dye	λ_{\max}^a (nm)	ϵ_{\max}^a (M ⁻¹ cm ⁻¹)	μ_{eg}^2 ^a (D ²)	$\mu_{\text{eg}}^2 M^{-1a}$ (D ² mol g ⁻¹)	μ_{g}^b (D)	$\Delta\mu^b$ (D)	c^{2b} (1)	$E_{1/2,\text{ox}}^c$ (V)	$E_{1/2,\text{red}}^c$ (V)
1	539	46 100	86	0.22	8.7	3.8	0.40	0.68 ^d	-1.61
2	576	66 400	98	0.23	6.2	4.2	0.40	0.65	-1.52
3	579	52 400	82	0.20	8.2	3.0	0.43	0.61 ^d	-1.58 ^d
4	584	60 200	89	0.20	7.7	3.2	0.42	0.63 ^d	-1.57 ^d
5	570	69 500	103	0.25	5.9	11.2	0.24	0.66	-1.38 ^d
6	577	64 200	94	0.26	9.1	4.4	0.39	0.55	-1.53 ^d
7	595	61 900	82	0.22	3.9	8.9	0.26	0.84 ^d	-1.18 ^d
8	675	91 200	97	0.23	4.8	7.7	0.42	0.61 ^d	-1.18
9	496	114 600	94	0.25	3.8	3.8	0.40	0.61 ^d	-1.94

^aUV–vis: CH₂Cl₂, ~10⁻⁵ M, 298 K. ^bEOA: 1,4-dioxane, ~10⁻⁶ M, 298 K, with Onsager cavity field correction to give gas-phase dipole moments.³⁷
^cCV: CH₂Cl₂, ~10⁻⁴ M, using Fc/Fc⁺ as an internal reference and NBu₄PF₆ as the electrolyte. ^dPeak potential of irreversible redox process.

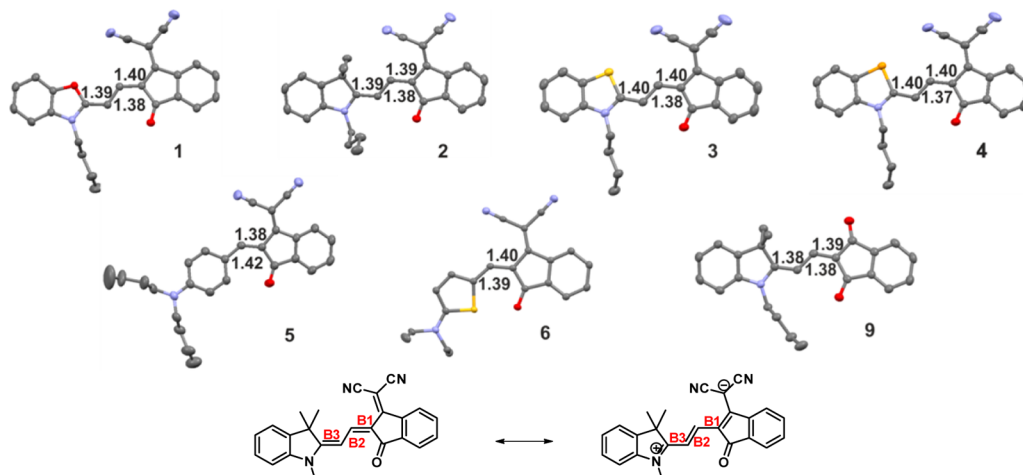


Figure 2. Top: Single-crystal structure of dyes 1–6 and 9 and the corresponding methine bridge bond lengths measured in the single crystals. Bottom: Polyene-like (left) and zwitterionic (right) structures of merocyanine dyes and the corresponding polymethine chain bonds, B1–B3, used to calculate the BLA.

Regarding the electrochemical properties, only (1-alkyl-3,3-dimethylindolin-2-ylidene)-containing dye **2** shows both reversible oxidation and reduction waves. The difference between the electrochemical gap determined from the redox potentials and the optical gap determined from the UV–vis absorption maxima was, in all cases, below 0.2 eV, thus implying that the $S_0 \rightarrow S_1$ transition observed in the UV–vis spectra corresponds to an electronic excitation from the HOMO to the LUMO level. Indeed, this difference would vanish for these merocyanine dyes if the onsets of the absorption bands would be used instead, which are about 30–50 nm bathochromically shifted with respect to the absorption maximum. The corresponding FMO levels were calculated taking an Fc/Fc⁺ value of -5.15 eV vs vacuum³⁵ and the optical gap. All compounds, with the exception of dye **7**, which shows very low-lying FMO levels, have HOMO levels in the range of 5.70–5.83 eV. Thus, when comparing their solar cell performance, similar open-circuit voltage (V_{OC}) values are expected. With regard to charge separation at the donor–acceptor heterojunction, most dyes show LUMO levels of about 3.53–3.65 eV, therefore providing the required 0.3 eV driving force to overcome the exciton binding energy.³⁶ For **7** and **8**, the driving force is only 0.2 eV; thus, charge transfer will occur with a reduced probability, and the influence of polarization effects in the solid state and local packing

arrangements may become influential on the charge separation thermodynamics and kinetics of these two dyes. A larger band gap that translates into a higher LUMO level is observed for dye **9** due to the shorter conjugation path of 1,3-indanedione. Accordingly, the charge separation process is expected to be efficient, whereas higher voltage losses will arise from the large energy offset between the LUMO levels of the donor and acceptor materials.

Bond Length Alternation (BLA). Depending on the strength of the respective donor and acceptor substituents, merocyanines can exist as a resonance structure of two formal states: the polyene-like form and the zwitterionic one (Figure 2). A hint regarding the contribution of each of these structures is provided by the BLA of the (tri)methine bridge. For a neutral polyene-like structure, bonds **B1** and **B3** are expected to be shorter than **B2**, and vice versa for the zwitterionic form.³⁸

Crystal structures could be obtained and analyzed for the majority of the dyes described in this study. The corresponding bond lengths are shown in Figure 2. The experimentally obtained BLA, defined as $\text{BLA} = R(\text{C}=\text{C}) - R(\text{C}-\text{C})$, where $R(\text{C}-\text{C})$ and $R(\text{C}=\text{C})$ correspond to the bond lengths of **B2** as well as of **B1** and **B3**, respectively (Table S2). As a general trend, **B2** was found to be slightly shorter than **B1** and **B3**, thus indicating a higher contribution of the zwitterionic form in the solid state. The only exception to this is dye **5**, which showed a

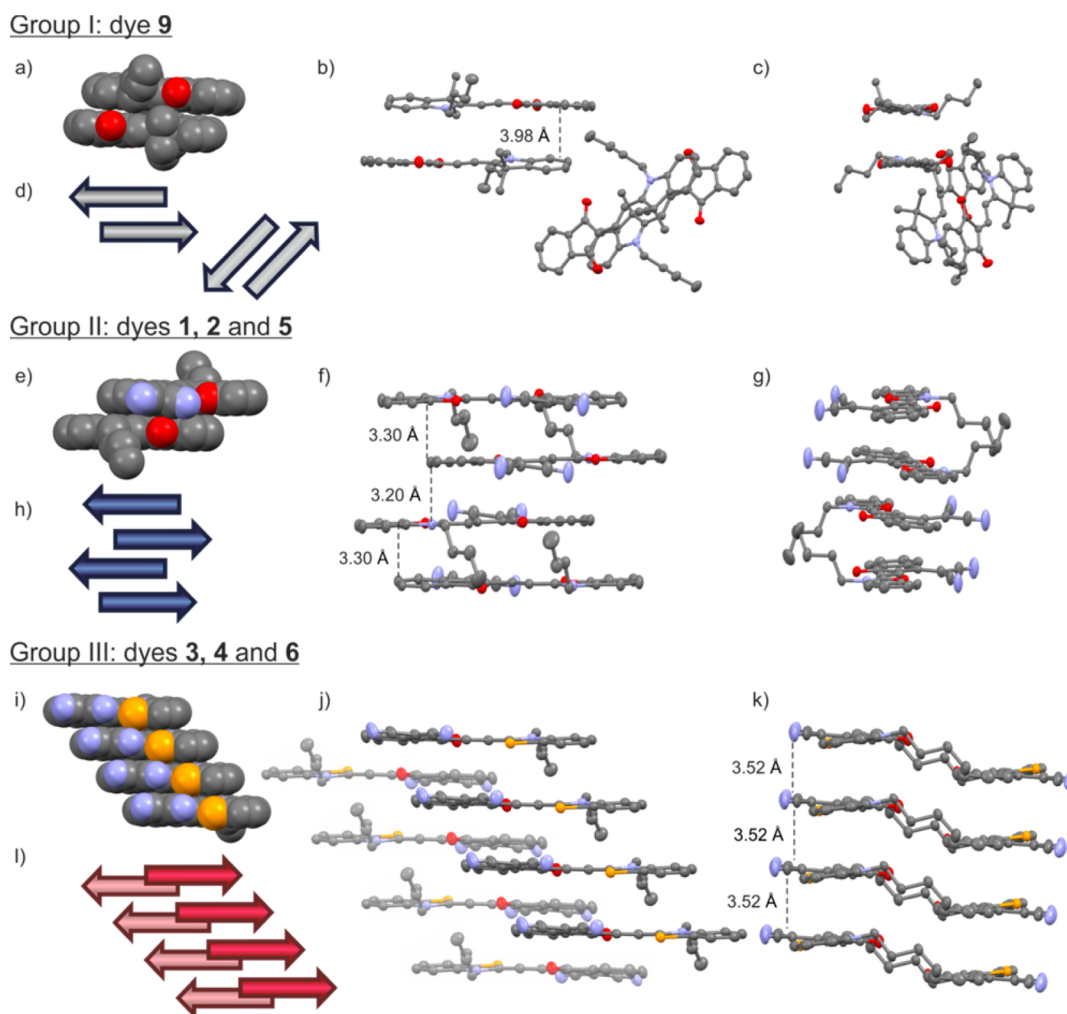


Figure 3. Packing motifs for merocyanine dyes based on single-crystal X-ray analyses. (a–d) Group (I), isolated dimers with no π -contact to the adjacent molecules: (a) space-filling view of a close dimer of 9, (b) side and (c) front views of neighboring dimers of 9 with an antiparallel packing motif, and (d) schematic representation of 9 showing the antiparallel orientation of the dipole moments (arrows) of the merocyanine dyes and their arrangement to the next neighboring dimer. (e–h) Group (II), one-dimensional stack of antiparallel dimers: (e) space-filling view of close dimer of 1, (f) side and (g) front views of the π -stack of 1 with an antiparallel packing motif, and (h) schematic representation of the π -stack of 1 showing the antiparallel orientation of the dipole moments (arrows) of the dyes and their unequal packing arrangement to the upper and lower neighbor dye. (i–l) Group (III), staircase-like arrangement: (i) space-filling view of the staircase-like packing of 4, (j) side and (k) front views of the π -stack of 4 with a staircase-like packing motif, and (l) schematic representation of the π -stack of 4 showing the parallel orientation of the dipole moments (arrows) and the equal distances to the upper and lower neighbors. In all panels, protons are omitted for clarity. Acceptor-to-acceptor plane distances are noted.

higher contribution of the polyene-like structure. Similar behavior is expected for dye 7; however, no crystal structure could be obtained for this dye. Since the bond length difference remained less than 0.04 Å for all measured dyes, it appears that all dyes exhibit an electronic structure close to the cyanine limit, which is known to provide the highest absorption strength and the fewest changes in bond length and molecular structure upon photoexcitation.³⁹

EOA experiments reveal that the situation in solution is slightly different. Thus, in the absence of the polarizing environment of the solid state, all molecules exhibit a ground state that is more polyene-like and an excited state that is more zwitterionic, as indicated by the increase of the dipole moment upon excitation (positive dipole difference $\Delta\mu$) and a c^2 value of less than 0.5. Two dyes (5, 7) are clearly polyene-like, with small c^2 values of around 0.25, whereas the other dyes already show a stronger transfer of charge from the donor to the

acceptor subunit in the ground state ($c^2 \geq 0.4$). The investigated dyes display dipole moments in the range 4–9 D.

Crystal Packing Analysis. Figure 3 shows the packing arrangements of representative dyes 1, 4, and 9.⁴⁰ The data of all of the obtained crystal structures can be found in Figure S9. The studied molecules show an almost planar π -scaffold, where the donor and acceptor units are slightly twisted out of the plane, with torsion angles varying from 3° for dye 1 to 15° for dye 5. Consequently, in order to obtain a meaningful comparison, the π - π distances were calculated from parallel planes of the acceptor moieties.

With regard to the relative arrangement between molecules, the dyes can be divided into three groups that vary in the dimensionality of the respective dye arrangement, as will be discussed below:

- (I) Centrosymmetric dimer units with no π -contacts to the neighboring molecules,

Table 2. Electrical Properties of OTFT Devices on Si/SiO₂ and Si/SiO₂/AlO_x/TPA Substrates Prepared by Vacuum Deposition and Measured in Air

dye	Si/SiO ₂				Si/SiO ₂ /AlO _x /TPA				
	T _S ^a (°C)	μ _p ^b (cm ² V ⁻¹ s ⁻¹)	I _{on} /I _{off} ^b (a.u.)	V _{th} ^b (V)	T _S ^a (°C)	μ _{max} ^c (cm ² V ⁻¹ s ⁻¹)	μ _p ^b (cm ² V ⁻¹ s ⁻¹)	I _{on} /I _{off} ^b (a.u.)	V _{th} ^b (V)
1	80	2.2 × 10 ⁻⁶ ± 0.6 × 10 ⁻⁶	2 × 10 ²	-16	80	7.2 × 10 ⁻⁶	6.7 × 10 ⁻⁶ ± 0.5 × 10 ⁻⁶	6 × 10 ²	+8
2	20 ^d	6.5 × 10 ⁻⁵ ± 0.3 × 10 ⁻⁵	4 × 10 ³	-6	20	No FE			
3	80	7.7 × 10 ⁻⁵ ± 0.5 × 10 ⁻⁵	5 × 10 ³	-7	80	0.035	0.032 ± 0.005	1 × 10 ⁵	-5
4	80	1.4 × 10 ⁻⁵ ± 0.5 × 10 ⁻⁵	1 × 10 ³	-1	80	0.080	0.077 ± 0.008	1 × 10 ⁵	-2
7	80	No FE			80	4.0 × 10 ⁻⁶	3.3 × 10 ⁻⁶ ± 0.9 × 10 ⁻⁶	3 × 10 ²	+3
9	20 ^d	3.2 × 10 ⁻⁶ ± 0.8 × 10 ⁻⁶	3 × 10 ²	-8	20	No FE			

^aSubstrate temperature. ^bAverage value of five randomly picked devices. ^cBest device. ^dAt elevated temperatures, dewetting of the thin films was observed.

- (II) a one-dimensional stack of slipped antiparallel dimer units featuring π -overlap with the neighboring molecules, (III) a one-dimensional staircase arrangement of parallel, highly slipped molecules with equidistant spacing.

Group (I), represented here by dye 9 (Figure 3a–d), is characterized by dimer units of antiparallel molecules with no overall dipole moment. In the case of dye 9, the distance between adjacent molecules within the dimer is 3.98 Å. The neighboring dimer unit is rotationally displaced; thus, any contact between the π -surfaces is hindered. Group (II), represented by dyes 1, 2, and 5 (Figure 3e–h; Figure S9a–d; Figure S9i–l), arranges in centrosymmetric dimers, where each molecule is slightly slipped over the next one, and presents a close and a distant neighbor, similar to the packing of previously reported merocyanines with 2-aminothiophene electron donor units.¹⁶ For dye 1, the π - π -distance between close neighbors is extremely short (3.20 Å), resulting in a much larger longitudinal slip than that between the distant neighbors. Interestingly, while the packing arrangement of dyes 2 and 5 shows a π -stack with alternating orientations of the dicyanovinyl groups, for dye 1, these are found to group in pairs, thus creating a lateral dipole moment that is annulated by the neighboring pair of molecules. Dyes 2 and 5 show larger distances (3.46 Å) between close neighbors (see Figure S9). This group of dyes is thus characterized by a one-dimensional π -stack of dimers, which should provide a good contact area between π -surfaces and enable charge percolation pathways to exist in at least one dimension in the solid state.

Finally, group (III), represented by dyes 3, 4, and 6 (Figure 3i–l), was found to pack in a completely new arrangement for dipolar compounds. The dyes are equidistant to the upper and lower neighbors, with dipole moments that are parallel to each other in a staircase-like arrangement. Near the first stair, a second one with an oppositely directed dipole moment appeared. This network follows a herringbone pattern. The π - π distance varies from 3.41 Å (6) to 3.50 Å (3) to 3.52 Å (4). The effect of the alkyl chains on the longitudinal displacement of neighboring stairs is more pronounced for dyes 3 and 4, bearing butyl chains. Ethyl-substituted dye 6 shows an almost equidistant distribution of the stairs. A deeper analysis of the staircase-like packing arrangement will be presented in the Discussion.

Organic Thin-Film Transistors. In order to study the charge carrier mobilities of the synthesized dyes, OTFTs on two different substrates were fabricated in a bottom-gate, top-contact configuration. The dyes were thermally evaporated in vacuum with a nominal thickness of 30 nm on top of Si/SiO₂

and Si/SiO₂/AlO_x/*n*-tetradecylphosphonic acid (TPA) substrates. During the sublimation of some dyes, the substrates were heated to elevated temperatures to induce a more crystalline film growth. The transfer characteristics of the devices were measured under ambient conditions for a drain-source voltage of $V_{DS} = -50$ V. Determination of the charge carrier mobility μ_p as well as the threshold voltage V_{th} was carried out using eq 1, which is valid for the saturation regime:⁴¹

$$\mu_p = (2I_{DS}L/[WC_i(V_{GS} - V_{th})^2]) \quad (1)$$

Here, I_{DS} describes the drain-source current, and C_i the capacitance of the dielectric, whereas L and W represent the length and width of the transistor channel, respectively. For every merocyanine, the electrical parameters were averaged over at least five OTFTs and showed a variation of less than 10%. The resulting hole mobilities, on–off ratios (I_{on}/I_{off}), and threshold voltages of the OTFTs of molecules 1–4, 7, and 9 on Si/SiO₂ and TPA-modified Si/SiO₂/AlO_x substrates can be found in Table 2. Dye 5 decomposed during sublimation, whereas thin films of 6 and 8 showed no OTFT performance. Representative transfer curves of the OTFTs on TPA-modified Si/SiO₂/AlO_x substrates can be found in Figures S11 and S12. Thin films of dyes 1–4 and 9 processed on Si/SiO₂ substrates all exhibited similar low charge carrier mobilities in the range of $\mu_p \approx 10^{-5}$ to 10^{-6} cm² V⁻¹ s⁻¹ in OTFT devices. In accordance with an earlier study for another series of merocyanine dyes, the low mobility values can be attributed to the formation of amorphous thin films.⁴⁰ Moreover, the fact that dyes 6–8 showed no field effect behavior on Si/SiO₂ substrates can be explained by the formation of small discontinuous droplet-like regions.⁴⁰ Hence, no percolation pathways are provided for charge carrier transport.

On the other hand, devices on TPA-modified Si/SiO₂/AlO_x substrates can be divided into two groups. Dyes 1 and 7 gave OTFTs with low mobilities in the range of 10^{-6} cm² V⁻¹ s⁻¹, whereas the mobility values for the devices with dyes 3 and 4 were significantly better than those on Si/SiO₂ substrates, with values of up to 0.08 cm² V⁻¹ s⁻¹ for dye 4. Likewise, the I_{on}/I_{off} are rather low for dyes 1 and 7, with values of the order of 10² whereas they reach up to 10⁵ for dyes 3 and 4. When comparing the threshold voltages, it can be seen that the devices with low mobility values (dyes 1 and 7) show positive threshold voltages of +8 and +3 V, respectively, which indicates that the OTFTs are already in the on-state due to trap states, although there is no applied bias voltage. In contrast, devices with high mobility values (dyes 3 and 4) feature negative

threshold voltages of -5 and -2 V, respectively, as expected for devices that are in the off-state when no bias voltage is applied. The above stated results can be rationalized by means of AFM measurements (see Figure S13).

The fact that devices composed of dyes 2, 6, 8, and 9 on TPA-modified Si/SiO₂/AlO_x substrates did not show any field effect can again be attributed to a dewetting of the substrates. The AFM results of the thin films of dyes 1 and 7 are counterintuitive to the low mobility values of the respective devices, as clear defined structures can be seen. Here, one would expect high mobility values due to crystalline thin films. However, as the nominal thickness of the films is only 30 nm, the films appear to be very rough with height maxima of 300 nm (dye 7) or even 500 nm (dye 1). Hence, XRD experiments were performed to investigate the crystallinity of the films. Regarding dye 7, only two very weak peaks were detected, which could not be assigned due to the lack of a single-crystal structure (Figure S14). In contrast, dye 1 featured two diffraction peaks of low intensity (Figure S15) that could be attributed to signals of the powder diffraction pattern simulated from our single-crystal data with the program Mercury.⁴² However, the low intensity of the peaks indicates only small crystalline regions with no preferential orientation with respect to the substrate. Therefore, the AFM and XRD results lead us to the conclusion that the low mobility can be attributed to rough amorphous regions between crystal grains, which are not favorable for charge transport.

The best mobilities of $\mu_p = 0.03$ and 0.08 cm² V⁻¹ s⁻¹ were obtained for devices based on dyes 3 and 4, respectively. From our AFM results, it appears that the films of both dyes display high crystallinity, as they feature terrace-like structures. The step heights are 2.4 nm for dye 3 and 2.2 nm for dye 4, whereas both films show grain sizes of about 1–2 μ m. The high crystallinity of the films of dye 4 has been confirmed with XRD measurements, which show many diffraction peaks of high intensity and with a sharp line width (Figures 5 and S16). The diffraction peaks correlate well with the (*h*00) signals obtained from the powder diffraction pattern simulated from our single-crystal data. The orientation of the molecules on the TPA-modified Si/SiO₂/AlO_x substrate was calculated from these data. The molecules adopt an edge-on packing, with the π - π stacking direction parallel to the substrate surface (Figure S16).

Summarizing, our studies show that the variation of the heteroatom in the donor part of dyes 1–4 has a pronounced impact on the formation of crystalline films and subsequently on the charge carrier mobility in OTFTs. While a dewetting of the substrate occurred for the C(Me)₂ group in dye 2, its replacement by an oxygen atom (dye 1) lead to the formation of closed films. Unfortunately, these showed only low crystallinity and were, therefore, not suitable for providing high charge carrier mobilities. Finally, if the C(Me)₂ group was replaced by a sulfur or selenium atom (dyes 3 and 4), then smooth crystalline films were formed and high charge carrier mobilities up to $\mu_p = 0.08$ cm² V⁻¹ s⁻¹ could be achieved for dye 4.

Solar Cells. Bulk heterojunction (BHJ) solar cells with the general architecture ITO/MoO₃ (15 nm)/MC:C₆₀ (50 nm, ratio 1:1)/Bphen (6 nm)/Ag (120 nm) were fabricated by thermal evaporation, in analogy to the OTFT devices. Due to its decomposition (see above), dye 5 was not included in this study.

The current–voltage (*J*–*V*) responses of the fabricated cells were measured under a nitrogen atmosphere and simulated AM

1.5 G irradiation (Figure 4). The corresponding data were averaged over at least 10 solar cells, showing a standard

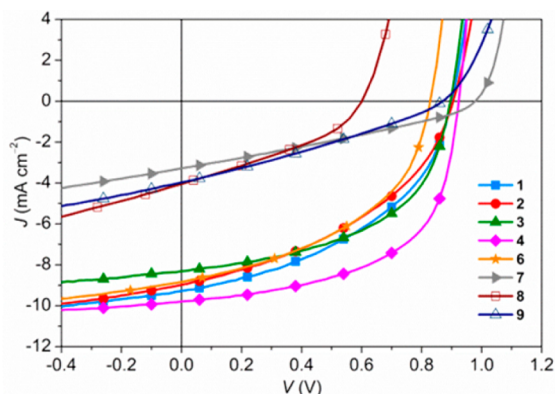


Figure 4. Overview of *J*–*V* responses measured under simulated solar irradiation (AM 1.5 G, 100 mW cm⁻²) of BHJ solar cells fabricated with dyes 1 (blue), 2 (red), 3 (green), 4 (pink), 6 (orange), 7 (gray), 8 (brown), and 9 (dark blue) as donor material and C₆₀ as acceptor material.

deviation below 5% (Table 3). The *V*_{OC}, which varied in the range of 0.6–1.0 V, correlated well with the HOMO energies of the dyes determined by CV measurements, in agreement with several recent publications.^{43,44} Indeed, dye 7, bearing the lowest HOMO level (-5.99 eV), showed the largest *V*_{OC} of 0.99 V.

Since most of the studied dyes have similar absorption profiles and HOMO/LUMO gaps, it is reasonable to expect similar short-circuit currents (*J*_{SC}). Indeed, for dyes 1–6, *J*_{SC} values of about 9 mA cm⁻² were obtained. These *J*_{SC} were in accordance with the calculated short-circuit currents calculated from the EQE spectra, since deviations below 10% were obtained (Table 3). Dyes 7–9, however, showed much lower *J*_{SC} values. In the case of dyes 7 and 8, the low *J*_{SC} might be rationalized by the fact that their low-lying LUMO might hinder efficient charge generation with C₆₀ as an acceptor material due to the lack of a driving force. Only for an offset of at least 0.3 eV,^{44,45} which is the case for dyes 1–6, can the exciton binding energy be overcome and the charge separation be efficient. On the other hand, the low *J*_{SC} of devices based on dye 9 may be influenced by its less favorable packing arrangement (Figure 3). Indeed, the low order of the packing adopted by 9 can lead to a high geminate recombination rate and therefore to a strong voltage-dependent photocurrent (Figure 4). Furthermore, the larger band gap of dye 9 limits the absorbed photons to higher energies (see Figure 1).

The highest variation among the investigated dyes was found in the fill factor (FF), which ranged from 0.30 to 0.56. The lowest values were obtained for dyes 7–9, possibly due to the low order of the films. Dyes 1, 2, and 6 showed FF in the range 0.42–0.46, whereas 3 and 4 displayed the highest FF of 0.52 and 0.56, respectively.

Although we assume that the morphology in the OTFTs and OSCs is significantly different (neat film vs bulk heterojunction), the correlation between the high mobility in the OTFT devices fabricated with dyes 3 and 4 and the remarkably good FF achieved is striking with respect to BHJ cells of other merocyanine dyes. This is indicative of related dye arrangements in both types of devices, leading to favorable charge transport properties within the donor phase and implies a more

Table 3. Optical Parameters for the Vacuum-Deposited Blends and Main BHJ Solar Cell Parameters

dye	λ_{max}^a (nm)	V_{OC}^b (V)	J_{SC}^b (mA cm ⁻²)	FF ^b (1)	PCE ^b (%)	$J_{\text{SC,EQE}}^c$ (mA cm ⁻²)
1	565	0.90 ± 0.01	9.2 ± 0.2	0.45 ± 0.01	3.7 ± 0.1	8.6
2	606	0.90 ± 0.01	9.0 ± 0.1	0.42 ± 0.01	3.4 ± 0.1	8.5
3	608	0.90 ± 0.01	8.2 ± 0.5	0.52 ± 0.01	3.7 ± 0.2	7.9
4	616	0.93 ± 0.01	10.0 ± 0.6	0.56 ± 0.03	5.2 ± 0.2	10.2
6	596	0.83 ± 0.01	8.8 ± 0.2	0.46 ± 0.01	3.4 ± 0.1	9.6
7	640	0.98 ± 0.01	3.4 ± 0.1	0.31 ± 0.01	1.0 ± 0.1	<i>d</i>
8	724	0.60 ± 0.01	3.8 ± 0.2	0.35 ± 0.01	0.8 ± 0.1	<i>d</i>
9	508	0.87 ± 0.01	3.7 ± 0.2	0.30 ± 0.01	1.0 ± 0.1	<i>d</i>

^aAbsorption maximum in the blend with C₆₀. ^bAverage values of ten BHJ solar cells. ^cIntegral current density values obtained from EQE measurements. ^dEQE spectrum not recorded.

balanced transport of electrons and holes in the solar cells, thus leading to higher FF.

In summary, on one hand, dyes 7–9 gave BHJ solar cells with poor efficiency. This is mainly attributed to unsuitable energy levels, which either did not provide the necessary driving force for exciton dissociation (dyes 7 and 8) or suffered from high energy losses while limiting absorption to higher photon energies (dye 9). On the other hand, dyes 1–6, which displayed ideally placed energy levels, showed satisfactory performances. In particular, selenium-containing dye 4 provided the best combination of absorption properties and supramolecular ordering, thus affording the best PCE of 5.2%.

Taking advantage of our OTFT results on molecular structure/packing and mobility, a cell optimization could be performed for the OSC based on dye 4 by introducing neat contact layers of the corresponding donor and acceptor materials above and below the active layer (mixed heterojunction, MHJ). The fabricated cell displays the following architecture: ITO/MoO₃ (15 nm)/dye 4 (3 nm)/dye 4:C₆₀ (50 nm, ratio 1:1)/C₆₀ (5 nm)/Bphen (6 nm)/Ag (120 nm). For comparison, a planar heterojunction solar cell (PHJ) with the structure ITO/MoO₃ (15 nm)/dye 4 (10 nm)/C₆₀ (30 nm)/Bphen (6 nm)/Ag (120 nm) was fabricated. The *J*–*V* characteristics of the MHJ, PHJ, and reference BHJ solar cells are listed in Table 4. The reference BHJ solar cell, described

Table 4. Solar Cell Characteristics of the Standard BHJ Solar Cell Compared with the PHJ and MHJ Solar Cells Based on Dye 4, Measured under Simulated AM 1.5 G Irradiation

device	processing	V_{OC}^a (V)	J_{SC}^a (mA cm ⁻²)	FF ^a (1)	PCE ^a (%)
BHJ	as grown	0.92	9.8	0.58	5.2
PHJ	as grown	0.98	4.9	0.49	2.2
	post annealing 2 min at 130 °C	0.30	4.7	0.49	0.7
MHJ	as grown	0.92	12.0	0.51	5.6
	post annealing 2 min at 130 °C	0.93	11.7	0.57	6.2

^aValues obtained for a solar cell of each type. As grown cells were deposited by sublimation on a substrate held at room temperature. The solar cell parameters were measured once before and after annealing at 130 °C for 2 min.

above, showed a PCE of 5.2%. The PHJ solar cell, on the other hand, showed a PCE of 2.2%. The introduction of donor and acceptor neat layers on both sides of the BHJ active layer, respectively, led to an improvement of performance up to 5.6% due to an enhancement of J_{SC} . In the case of MHJ devices, the postproduction thermal annealing led to a strong enhancement

of performance translated in power conversion efficiencies up to 6.2%.

The as grown MHJ showed an increased J_{SC} but a lower FF in comparison to those of the reference BHJ solar cell. In our previous studies on BHJ solar cells, postproduction thermal annealing had no influence on cell performance.⁴⁶ However, the investigation of OTFTs with dye 4 described above and previous studies of annealing on the performance of PHJ devices⁴⁷ suggested that postproduction annealing should be applied to the MHJ device in order to recover the FF. A similar improvement in solar cell performance of other small molecule donor materials as a consequence of thermally favored solid-state packing has been reported.^{48,49} After an annealing procedure of 2 min at 130 °C on a hot plate, the MHJ still showed a very high J_{SC} in addition to a FF that equals that of the reference BHJ cell, thus leading to an overall improvement of performance to 6.2%. The neat and thermally annealed film of dye 4 in optimized MHJ solar cells has two functions: First, contact of the electron acceptor, C₆₀, with the hole-collecting MoO₃ layer is avoided, which reduces surface recombination. Second, the transport of charge carriers to the hole collection contact is accelerated. As a result, the MHJ solar cell shows an enhancement in PCE in comparison to that of the reference BHJ solar cell by introducing only 3 nm of selenium-containing dye 4.

Moreover, the impact of thermal annealing in the optimized MHJ based on 4 bearing 6.2% PCE has been analyzed in detail. For this purpose, grazing incident X-ray scattering as well as ellipsometric and AFM measurements were performed. In Figure 5a, the grazing incident X-ray pattern of a neat dye 4 thin film (solid lines) as well as dye 4:C₆₀ blend (dotted lines) deposited on glass substrates before and after annealing is shown. As grown films of both neat dye 4 and the dye 4:C₆₀ blend do not show any pronounced features, whereas annealing at 130 °C for 2 min led to the formation of peaks for the neat dye 4 film. Comparing the peaks with the single-crystal data allows them to be assigned to the (*h*00) orientation. The slight shift of the measured peak positions compared with the simulated data from the single-crystal structure is a consequence of the different temperatures applied for single-crystal and thin-film measurements as well as a possible tilting of the unit cell with respect to the substrate. Thus, our findings indicate a high degree of order in the neat film. AFM and UV–vis measurements confirmed the reorganization and ordering upon annealing of dye 4 molecules in neat thin films, giving rise to very crystalline domains of 1–2 μm (Figure S18). Moreover, the UV–vis absorption spectrum of the BHJ solar cell based on dye 4 was compared to the spectra of thin films on quartz and reflective Si/Al/AIO_x/TPA substrates, as well as with the

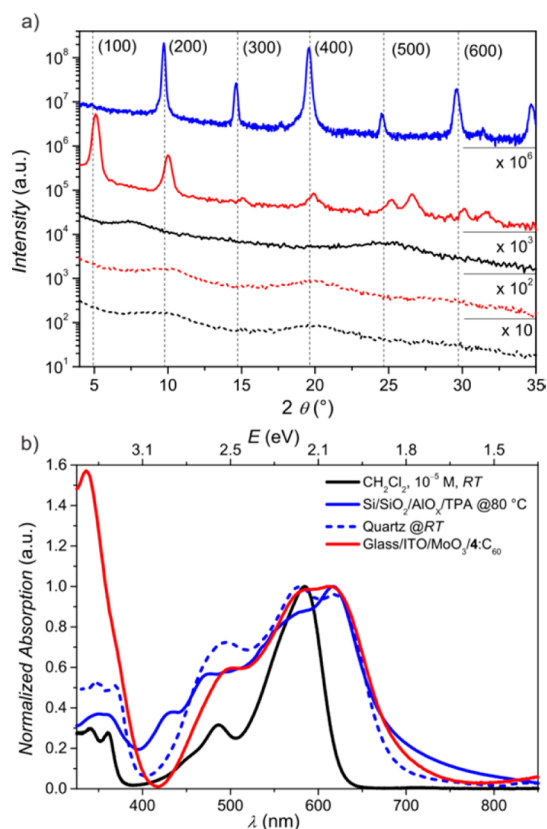


Figure 5. (a) X-ray pattern of a neat thin film of dye 4 (solid lines) and its mixture with C_{60} (dotted lines) on glass substrates as grown (black, substrate at room temperature) and after thermal annealing (red) at 130 °C for 2 min. For comparison, the X-ray diffractogram of dye 4 deposited on heated Si/Al/AlO_x/TPA substrate (blue line) is shown. (b) Comparison of UV-vis spectra in CH₂Cl₂ (black, $\sim 10^{-5}$ M), vacuum-deposited thin film on heated reflective Si/Al/AlO_x/TPA substrate (solid blue line), vacuum-deposited thin film on nonheated quartz (dashed blue line), and the corresponding solar cell (50% C_{60} , red line) for dye 4.

molecular absorption in solution (Figure 5b). For this purpose, thin films on quartz were deposited in order to obtain amorphous films (high deposition rate and substrate at RT), whereas thin films on TPA-modified substrates were fabricated like the films used for OTFT in order to obtain higher crystallinity (low deposition rate and elevated substrate temperature), which could be confirmed by X-ray analysis. In Figure 5b, a comparison of these UV-vis spectra and those in dichloromethane solution are shown for compound 4. The solar cell spectrum, depicted in red, shows the characteristic absorption of C_{60} at ~ 350 nm. Furthermore, a general broadening of the solid-state absorption spectra with respect to solution is observed as well. Interestingly, dye 4 shows spectra centered at about 650 nm with remarkably small changes between the neat thin films and the solar cell spectrum.

DISCUSSION

In this section, the influence of various parameters ranging from molecular properties to the packing in the solid state on BHJ solar cell efficiency is analyzed. Starting with the molecular properties of the studied dyes, we find similar absorption in the 450–650 nm region for compounds 1–7, resulting in similar J_{SC} values. Compounds 8 and 9, on the other hand, show red- and blue-shifted absorptions, respectively. Moreover, the energy

levels of dyes 1–6 are ideally located with respect to the LUMO level of C_{60} . Accordingly, little variation in V_{OC} was found for these materials. Although dyes 7 and 8 presented favorable absorption properties, the low-lying LUMO levels may have prevented efficient exciton dissociation into charge carriers, thus reducing the final photocurrent and consequently the solar cell performance. On the other hand, dye 9, with the largest optical gap, features a very high LUMO level, which would imply high energy losses by thermalization upon exciton dissociation. On the basis of these results and those from our earlier studies,^{15,16} we can conclude that for merocyanine dyes, whose lowest energy transition is attributable to a HOMO–LUMO transition, simple design rules can be applied to tailor the molecular properties for BHJ solar cells. These include an approximately 0.3 eV higher LUMO level of the dye compared to that of C_{60} and an intense absorption band in the visible range that requires a substitution of the polymethine chain by strong heterocyclic electron donor and acceptor units.

However, molecular properties alone are not sufficient to achieve high performance OSC and OTFT materials. Not only FF and J_{SC} but also V_{OC} is strongly influenced by the morphology, i.e., solid-state packing on a supramolecular level.⁵⁰ Merocyanine dyes tend to arrange in an antiparallel fashion due to dominant dipole–dipole interactions.¹⁶ The dimers formed in this manner are found to show different long-range order that varies from a higher ordered π -stacked network (group III) to isolated dimers that lack further π -contacts to their neighboring molecules (group I). The reason for adopting one packing or the other has been previously discussed in terms of steric hindrance.⁴⁰ Small substituents allow the molecules to perfectly pack in overlapping dimers with no overall dipole moment. Thus, for the next molecule, no electrostatic driving force is provided to direct subsequent antiparallel π -stacking, and therefore isolated dimers are more likely to be formed. This is the case for dye 9 (group I). On the other hand, sterically hindered molecules tend to form more slipped dimers, where the acceptor or donor moieties overlap, thus forming a dimer unit that is still slightly polarized and therefore favors the interaction with the next molecule, which is more likely to stack on top of the existing dimer. This is the case for dyes 1, 2, and 5 (group II). Finally, dyes 3, 4, and 6 arrange in a so far unprecedented staircase-like pattern of translationally displaced dyes where the dipole moments are not balanced within the π -stack (group III). Accordingly, the parallel slipped π -stack of the closest neighbors builds a macrodipole that is balanced only by the neighbor staircase stacks that are oriented in the opposite direction. The fact that three dyes, all showing good performance in BHJ solar cells and two of them showing good performance in OTFTs, arrange similarly in such an unusual packing motif is indeed striking.

DFT calculations were performed in order to visualize the electrostatic surface potential of the isolated monomers (see Figures S20 and S21) of 1 and 4 as well as the different packing arrangements found in the crystal structure (Figure 6). For this purpose, the geometry of the molecules was taken from the single-crystal structure, and a single-point energy optimization (B3-LYP^{51–53} 6-31G(d), Gaussian⁵⁴) was performed. For dye 1 (Figure 6c), the stacking of the molecules creates a polarized ensemble with higher electron density in the center, where the acceptor groups are placed on top of each other, whereas lower electron density is found on the donor units. On the other hand, compound 4 presents two relative stair–stair arrangements (Figure 6b). The longitudinal displacement is smaller for

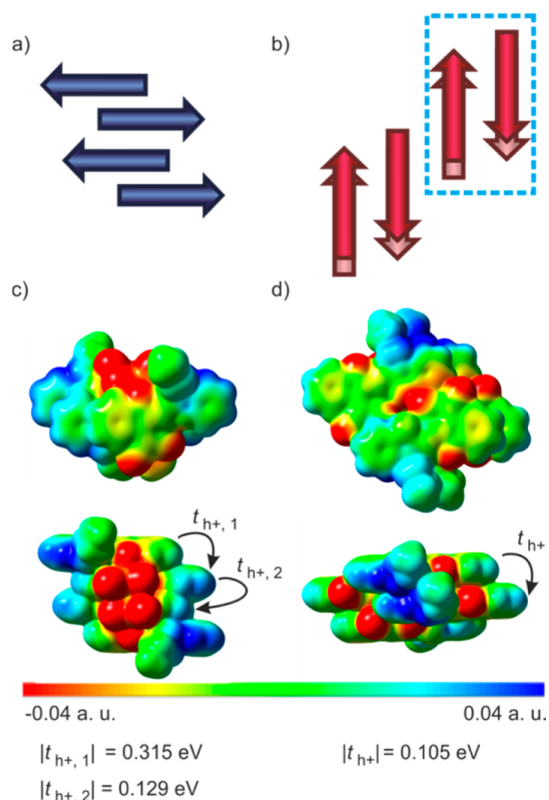


Figure 6. Schematic representation of the π -stack of dye 1 (a) and the staircase-like arrangement of dye 4 (b) in the crystal indicating the orientation of the dipole moments (arrows). The corresponding electrostatic surface potential (top, top view; bottom, side view) calculated from the crystal geometry taking an isovalue of 0.001 is depicted for dyes 1 (c) and 4 (d). For 4, the stair–stair arrangement contained in the blue rectangle was taken for the calculations. The values of the calculated charge transfer integrals are depicted as well.

the arrangement in which the alkyl chains are oriented to the outer side (blue rectangle in Figure 6b). In this arrangement, each donor unit is facing an acceptor unit, which results in a less polarized system than that of the isolated monomer. This antiparallel arrangement of the stairs thus ensures the overall charge balancing of the crystal (stair-dimer). The reason that these dyes tend to pack in a staircase-like arrangement instead of forming dimers is still unclear; however, selenium is known to have a strong Lewis acid character, and its interactions with halogen and nitrile groups have been previously reported.^{55,56} The electrostatic potential surface in Figure 6d shows, indeed, a reddish area at the selenium position near the nitrile group, thus suggesting some kind of electronic density lying on the Se atom. If we take into account the small intermolecular N–Se distance (3.60 Å) found in the crystal, then it seems reasonable to explain the adopted packing structure by CN–Se electrostatic interactions.⁵⁶

Furthermore, the charge transfer integrals for the close and distant neighbors of dye 1 as well as for the staircase-arranged dye 4 were calculated. The corresponding transfer integral values are depicted in Figure 6c,d. The calculations show very balanced charge transport for dye 4 within the staircase stack. Moreover, dye 1 showed even higher transfer integral values for the close dimer ($t_{h+,1}$) and similar values for the far dimer ($t_{h+,2}$). This is, however, not reflected by transistor measurements. Close inspection of the AFM image of dye 1 (Figure S13) offers a clue to this apparent discrepancy. The irregular

growth of the films gives rise to a large number of grain boundaries with amorphous regions connecting them. Thus, the mobility in films of dye 1 is rather limited by these defects. Indeed, transistor devices, which are composed of a neat layer of organic material, are extremely sensitive to molecular ordering.⁵⁷ This is in agreement with theoretical calculations of charge transfer integrals in oligoacenes and rubrene, which are prototypical examples of OTFT materials that crystallize in a herringbone arrangement. The slight displacement of cofacial rubrene dimers increases the charge transfer integrals, leading to higher mobility.^{58,59} It is thus quite evident that the high mobilities of 0.03 and 0.08 $\text{cm}^2 \text{V}^{-1} \text{s}^{-1}$ for dyes 3 and 4, respectively, relates to the particular arrangement in the crystal.

In BHJ solar cell devices, crystallinity and orientation of the dyes influence all performance parameters such as V_{OC} , J_{SC} , and FF. However, mixing donor and acceptor materials reduces the overall ordering of the active layer and the domain size and, therefore, it is not straightforward to predict the effect of ordering on V_{OC} .⁵⁰ A good estimate of V_{OC} for the active layer in the BHJ is the difference between the HOMO of the dye and the LUMO of C_{60} . Because of their similar HOMO levels, it is not surprising that dyes 1–6 show similar V_{OC} . On the basis of this simple estimate, V_{OC} values of dyes 4 and 8 are expected to be similar; however, they differ by 0.3 V, pointing to the importance of supramolecular order and morphology.⁶⁰ Within this series, dyes 1, 2, and 4 show the highest absorption in films of equal thickness in a blend with C_{60} . The differences with respect to absorption in solution might be due to polarization as well as exciton coupling effects in the solid state. The high absorption of dyes 1 and 4, together with the favorable calculated charge transfer integrals, correlate well with the J_{SC} values found for the corresponding solar cells, which are the highest in this series. Since the FF is influenced by charge generation and recombination (transport), it benefits most from a proper supramolecular order and crystallinity and thus from a high mobility, as has been demonstrated to be superior for dye 4 in OTFT studies.

Since the AFM images and X-ray analyses of thin films of 4 on TPA-modified $\text{Si}/\text{SiO}_2/\text{AlO}_x$ substrates clearly showed crystalline terrace-like growth, we can assume that the corresponding absorption spectra has the signature of highly ordered molecules with a packing arrangement that is similar to the one in the single crystal (although with a smaller domain size and more disorder). The thin-film spectra showed, in all cases, a characteristic red-shifted band with respect to the solution spectrum (Figure 5). Such a bathochromically shifted absorption peak can be attributed to J -type coupling between the closely π -stacked dyes, in accordance with the packing arrangement in the single crystal, i.e., staircase stack slip of $\theta < 50^\circ$.⁶¹ While recent research indicates that high exciton mobilities may be possible for other arrangements of π -stacked dyes as well, e.g., even some H -aggregates,^{62,63} J -aggregation is still considered to enable the largest exciton mobilities and the least undesired nonradiative deactivation channels.^{64–66}

For this reason, we emphasize the similarity of the thin-film spectra for all devices shown for dye 4 in Figure 5b because they indicate the presence of similar local contacts between slipped stacked merocyanine 4 chromophores in neat films and in BHJ devices. This was notably not the case for most of the other dyes of the given series (Figure S19), which suggests that these dyes exhibit a less favored preference for a particular arrangement. Accordingly, domains composed of different dye arrangements may coexist for the other dyes, and their ratio

may depend on the deposition parameters, interactions with the substrate used, and the presence of C₆₀ fullerene.

CONCLUSIONS

In this work, we have presented a series of nine structurally related D–A merocyanine dyes bearing a 2-(3-oxo-2,3-dihydro-1H-inden-1-ylidene)malononitrile acceptor moiety linked to different donor units. On the molecular level, the reported chromophores display similar absorption properties in the 450–650 nm range, with the exception of dyes **8** and **9**, which show red- and blue-shifted absorptions, respectively. Furthermore, electrochemical measurements revealed favorable HOMO levels for obtaining V_{OC} values of about 1.0 V and LUMO levels that, with the exception of dyes **7** and **8**, should provide enough driving force for exciton dissociation at the D–A interface of BHJ solar cells. On the supramolecular level, the reported chromophores were found to arrange in three different packing motifs: group (I), represented by dye **9**, showed isolated antiparallel dimers with no π -contact to the neighboring molecules; group (II), composed of dyes **1**, **2**, and **5**, showed 1D π -stacks of antiparallel dimeric units; and group (III), to which dyes **3**, **4**, and **6** belong, arranged in staircase-like slipped parallel π -stacks within a herringbone structure. The latter packing arrangement was also found for dye **4** in thin films prepared on TPA-modified Si/SiO₂/AlO_x substrate. The hole mobility of dye **4** based OTFTs reached up to $\mu_p = 0.08 \text{ cm}^2 \text{ V}^{-1} \text{ s}^{-1}$. With respect to BHJ solar cell devices, dyes **1–6** showed PCE higher than 3.0%, whereas dyes **7–9** suffered from very low photocurrent. Among the solar cells, the one based on selenium-containing dye **4** featured the best PCE of this series (5.2%). The superiority of dye **4** devices is attributed to the slipped π -stacking packing motif (group III) and the J-type coupling with very high absorption displayed in the blend with C₆₀, together with the higher polarizability of selenium and the high charge carrier mobility found in OTFT devices.

Furthermore, an optimization of the solar cells based on selenium-containing merocyanine dye **4** and C₆₀ through addition of neat donor and acceptor films above and below the active layer as well as postprocessing annealing of the blend was performed, leading to a PCE of 6.2%. The resulting increase in performance was attributed to a high ordering of the neat layer of dye **4**, which was corroborated by XRD and UV–vis measurements. This mixed heterojunction solar cell is, accordingly, our best achievement after one decade of research on dipolar dye-based photovoltaic materials and constitutes the record holder among merocyanine dye-based organic solar cells.

ASSOCIATED CONTENT

Supporting Information

The Supporting Information is available free of charge on the ACS Publications website at DOI: 10.1021/jacs.5b06722.

Synthetic procedures, UV–vis and EOA spectra, CV measurements, OTFT as well as solar cell fabrication and characterization data, AFM images, single-crystal data, X-ray of films, DFT calculations, and ¹H NMR spectra (PDF).

Crystallographic data (CIF, CIF, CIF, CIF, CIF).

AUTHOR INFORMATION

Corresponding Authors

*(K.M.) klaus.meerholz@uni-koeln.de

*(F.W.) wuerthner@chemie.uni-wuerzburg.de

Notes

The authors declare no competing financial interest.

ACKNOWLEDGMENTS

This work was financially supported by the German Federal Ministry of Science and Education (BMBF) within the LOTSE (FKZ: 03EK3503C) and the MEDOS (FKZ: 03EK3505I) projects. We thank Drs. Hannah Bürckstümmer and Elena Tulyakova for the synthesis of some of the described dyes as well as Astrid Kudzus for processing some of the compounds. We thank Drs. Hagen Klauk and Ute Zschieschang (MPI für Festkörperforschung, Stuttgart) for providing us with TPA-modified Si/SiO₂/AlO_x substrates.

REFERENCES

- (1) Tang, C. W. *Appl. Phys. Lett.* **1986**, *48*, 183.
- (2) Zhou, J.; Zuo, Y.; Wan, X.; Long, G.; Zhang, Q.; Ni, W.; Liu, Y.; Li, Z.; He, G.; Li, C.; Kan, B.; Li, M.; Chen, Y. *J. Am. Chem. Soc.* **2013**, *135*, 8484.
- (3) Zhou, J.; Wan, X.; Liu, Y.; Zuo, Y.; Li, Z.; He, G.; Long, G.; Ni, W.; Li, C.; Su, X.; Chen, Y. *J. Am. Chem. Soc.* **2012**, *134*, 16345.
- (4) Liu, Y.; Chen, C. C.; Hong, Z.; Gao, J.; Yang, Y. M.; Zhou, H.; Dou, L.; Li, G.; Yang, Y. *Sci. Rep.* **2013**, *3*, 3356.
- (5) van der Poll, T. S.; Love, J. A.; Nguyen, T.-Q.; Bazan, G. C. *Adv. Mater.* **2012**, *24*, 3646.
- (6) Chao, Y. H.; Jheng, J. F.; Wu, J. S.; Wu, K. Y.; Peng, H. H.; Tsai, M. C.; Wang, C. L.; Hsiao, Y. N.; Wang, C. L.; Lin, C. Y.; Hsu, C. S. *Adv. Mater.* **2014**, *26*, 5205.
- (7) He, Z. C.; Zhong, C. M.; Su, S. J.; Xu, M.; Wu, H. B.; Cao, Y. *Nat. Photonics* **2012**, *6*, 591.
- (8) Kyaw, A. K.; Wang, D. H.; Wynands, D.; Zhang, J.; Nguyen, T.-Q.; Bazan, G. C.; Heeger, A. J. *Nano Lett.* **2013**, *13*, 3796.
- (9) Meerheim, R.; Körner, C.; Leo, K. *Appl. Phys. Lett.* **2014**, *105*, 063306.
- (10) Mishra, A.; Bäuerle, P. *Angew. Chem., Int. Ed.* **2012**, *51*, 2020.
- (11) Lin, Y.; Li, Y.; Zhan, X. *Chem. Soc. Rev.* **2012**, *41*, 4245.
- (12) Li, Y. W.; Guo, Q.; Li, Z. F.; Pei, J. N.; Tian, W. J. *Energy Environ. Sci.* **2010**, *3*, 1427.
- (13) Dieckmann, A.; Bäessler, H.; Borsenberger, P. M. *J. Chem. Phys.* **1993**, *99*, 8136.
- (14) Würthner, F.; Meerholz, K. *Chem. - Eur. J.* **2010**, *16*, 9366.
- (15) Kronenberg, N. M.; Deppisch, M.; Würthner, F.; Lademann, H. W.; Deing, K.; Meerholz, K. *Chem. Commun.* **2008**, *48*, 6489.
- (16) Bürckstümmer, H.; Tulyakova, E. V.; Deppisch, M.; Lenze, M. R.; Kronenberg, N. M.; Gsänger, M.; Stolte, M.; Meerholz, K.; Würthner, F. *Angew. Chem., Int. Ed.* **2011**, *50*, 11628.
- (17) Steinmann, V.; Kronenberg, N. M.; Lenze, M. R.; Graf, S. M.; Hertel, D.; Meerholz, K.; Bürckstümmer, H.; Tulyakova, E. V.; Würthner, F. *Adv. Energy Mater.* **2011**, *1*, 888.
- (18) Xia, P. F.; Feng, X. J.; Lu, J.; Tsang, S.-W.; Movileanu, R.; Tao, Y.; Wong, M. S. *Adv. Mater.* **2008**, *20*, 4810.
- (19) Cho, N.; Kim, J.; Song, K.; Lee, J. K.; Ko, J. *Tetrahedron* **2012**, *68*, 4029.
- (20) Ripaud, E.; Rousseau, T.; Leriche, P.; Roncali, J. *Adv. Energy Mater.* **2011**, *1*, 540.
- (21) Leliège, A.; Regent, C.-H. L.; Allain, M.; Blanchard, P.; Roncali, J. *Chem. Commun.* **2012**, *48*, 8907.
- (22) Choi, J. W.; Kim, C.-H.; Pison, J.; Oyedele, A.; Tondelier, D.; Leliège, A.; Kirchner, E.; Blanchard, P.; Roncali, J.; Geffroy, B. *RSC Adv.* **2014**, *4*, 5236.
- (23) Lin, H.-W.; Chiu, S.-W.; Lin, L.-Y.; Hung, Z.-Y.; Chen, Y.-H.; Lin, F.; Wong, K.-T. *Adv. Mater.* **2012**, *24*, 2269.
- (24) Leliège, A.; Grolleau, J.; Allain, M.; Blanchard, P.; Demeter, D.; Rousseau, T.; Roncali, J. *Chem. - Eur. J.* **2013**, *19*, 9948.

- (25) Chen, Y. H.; Lin, L. Y.; Lu, C. W.; Lin, F.; Huang, Z. Y.; Lin, H. W.; Wang, P. H.; Liu, Y. H.; Wong, K.-T.; Wen, J.; Miller, D. J.; Darling, S. B. *J. Am. Chem. Soc.* **2012**, *134*, 13616.
- (26) Bürckstümmer, H.; Kronenberg, N. M.; Gsänger, M.; Stolte, M.; Meerholz, K.; Würthner, F. *J. Mater. Chem.* **2010**, *20*, 240.
- (27) Ritzel, C.; Schmälzlin, E.; Bräuchle, C. R.; Meerholz, K.; Rössler, A.; Ernst, C.; Wichern, J. *Proc. SPIE* **1999**, 202.
- (28) Krause, S.; Stolte, M.; Würthner, F.; Koch, N. *J. Phys. Chem. C* **2013**, *117*, 19031.
- (29) Chehimi, M. M.; Delamar, M. J. *J. Electron Spectrosc. Relat. Phenom.* **1989**, *49*, 231.
- (30) Briseno, A. L.; Miao, Q.; Ling, M.-M.; Reese, C.; Meng, H.; Bao, Z.; Wudl, F. *J. Am. Chem. Soc.* **2006**, *128*, 15576.
- (31) Tucker, N. M.; Briseno, A. L.; Acton, O.; Yip, H.-L.; Ma, H.; Jenekhe, S. A.; Xia, Y.; Jen, A. K.-Y. *ACS Appl. Mater. Interfaces* **2013**, *5*, 2320.
- (32) Cerniani, A.; Passerini, R. *J. Chem. Soc.* **1954**, 2261.
- (33) Deligeorgiev, T. G.; Gadjev, N. I.; Drexhage, K. H. *Dyes Pigm.* **1991**, *15*, 215.
- (34) Davydenko, I. G.; Kachkovsky, A. D.; Dekhtyar, M. L.; Slominskii, Y. L.; Tolmachev, A. I. *J. Phys. Org. Chem.* **2010**, *23*, 96.
- (35) Cardona, C. M.; Li, W.; Kaifer, A. E.; Stockdale, D.; Bazan, G. C. *Adv. Mater.* **2011**, *23*, 2367.
- (36) Koster, L. J. A.; Mihailetchi, V. D.; Blom, P. W. M. *Appl. Phys. Lett.* **2006**, *88*, 093511.
- (37) Onsager, L. *J. Am. Chem. Soc.* **1936**, *58*, 1486.
- (38) Marder, S. R.; Perry, J. W. *Science* **1994**, *263*, 1706.
- (39) Würthner, F.; Wortmann, R.; Matschiner, R.; Lukaszuk, K.; Meerholz, K.; DeNardin, Y.; Bittner, R.; Bräuchle, C.; Sens, R. *Angew. Chem., Int. Ed. Engl.* **1997**, *36*, 2765.
- (40) Liess, A.; Huang, L.; Arjona-Esteban, A.; Lv, A.; Gsänger, M.; Stepanenko, V.; Stolte, M.; Würthner, F. *Adv. Funct. Mater.* **2015**, *25*, 44.
- (41) Sirringhaus, H. *Adv. Mater.* **2014**, *26*, 1319.
- (42) Macrae, C. F.; Edgington, P. R.; McCabe, P.; Pidcock, E.; Shields, G. P.; Taylor, R.; Towler, M.; van de Streek, J. *J. Appl. Crystallogr.* **2006**, *39*, 453.
- (43) Rand, B. P.; Burk, D. P.; Forrest, S. R. *Phys. Rev. B: Condens. Matter Mater. Phys.* **2007**, *75*, 115327.
- (44) Scharber, M. C.; Mühlbacher, D.; Koppe, M.; Denk, P.; Waldauf, C.; Heeger, A. J.; Brabec, C. *Adv. Mater.* **2006**, *18*, 789.
- (45) van Eersel, H.; Janssen, R. A. J.; Kemerink, M. *Adv. Funct. Mater.* **2012**, *22*, 2700.
- (46) Kronenberg, N. M.; Bürckstümmer, H.; Deppisch, M.; Würthner, F.; Meerholz, K. *J. Photonics Energy* **2011**, *1*, 011101.
- (47) Ojala, A.; Petersen, A.; Fuchs, A.; Lovrincic, R.; Pölking, C.; Trollmann, J.; Hwang, J.; Lennartz, C.; Reichelt, H.; Höffken, H. W.; Pucci, A.; Erk, P.; Kirchartz, T.; Würthner, F. *Adv. Funct. Mater.* **2012**, *22*, 86.
- (48) Fitzner, R.; Mena-Osteritz, E.; Mishra, A.; Schulz, G.; Reinold, E.; Weil, M.; Körner, C.; Ziehlke, H.; Elschner, C.; Leo, K.; Riede, M.; Pfeiffer, M.; Urich, C.; Bäuerle, P. *J. Am. Chem. Soc.* **2012**, *134*, 11064.
- (49) Paudel, K.; Johnson, B.; Thieme, M.; Haley, M. M.; Payne, M. M.; Anthony, J. E.; Ostroverkhova, O. *Appl. Phys. Lett.* **2014**, *105*, 043301.
- (50) Poelking, C.; Tietze, M.; Elschner, C.; Olthof, S.; Hertel, D.; Baumeier, B.; Würthner, F.; Meerholz, K.; Leo, K.; Andrienko, D. *Nat. Mater.* **2015**, *14*, 434.
- (51) Becke, A. D. *Phys. Rev. A: At., Mol., Opt. Phys.* **1988**, *38*, 3098.
- (52) Lee, C.; Yang, W.; Parr, R. G. *Phys. Rev. B: Condens. Matter Mater. Phys.* **1988**, *37*, 785.
- (53) Becke, A. D. *J. Chem. Phys.* **1993**, *98*, 5648.
- (54) Frisch, M. J.; Trucks, G. W.; Schlegel, H. B.; Scuseria, G. E.; Robb, M. A.; Cheeseman, J. R.; Scalmani, G.; Barone, V.; Mennucci, B.; Petersson, G. A.; Nakatsuji, H.; Caricato, M.; Li, X.; Hratchian, H. P.; Izmaylov, A. F.; Bloino, J.; Zheng, G.; Sonnenberg, J. L.; Hada, M.; Ehara, M.; Toyota, K.; Fukuda, R.; Hasegawa, J.; Ishida, M.; Nakajima, T.; Honda, Y.; Kitao, O.; Nakai, H.; Vreven, T.; Montgomery, J. A., Jr.; Peralta, J. E.; Ogliaro, F.; Bearpark, M.; Heyd, J. J.; Brothers, E.; Kudin,
- K. N.; Staroverov, V. N.; Kobayashi, R.; Normand, J.; Raghavachari, K.; Rendell, A.; Burant, J. C.; Iyengar, S. S.; Tomasi, J.; Cossi, M.; Rega, N.; Millam, J. M.; Klene, M.; Knox, J. E.; Cross, J. B.; Bakken, V.; Adamo, C.; Jaramillo, J.; Gomperts, R.; Stratmann, R. E.; Yazyev, O.; Austin, A. J.; Cammi, R.; Pomelli, C.; Ochterski, J. W.; Martin, R. L.; Morokuma, K.; Zakrzewski, V. G.; Voth, G. A.; Salvador, P.; Dannenberg, J. J.; Dapprich, S.; Daniels, A. D.; Farkas, O.; Foresman, J. B.; Ortiz, J. V.; Cioslowski, J.; Fox, D. J. *Gaussian 09*, revision D; Gaussian, Inc.: Wallingford, CT, 2009.
- (55) Beer, L.; Cordes, A. W.; Myles, D. J. T.; Oakley, R. T.; Taylor, N. J. *CrystEngComm* **2000**, *2*, 109.
- (56) Gsänger, M.; Kirchner, E.; Stolte, M.; Burschka, C.; Stepanenko, V.; Pflaum, J.; Würthner, F. *J. Am. Chem. Soc.* **2014**, *136*, 2351.
- (57) Dou, J.-H.; Zheng, Y.-Q.; Lei, T.; Zhang, S.-D.; Wang, Z.; Zhang, W.-B.; Wang, J.-Y.; Pei, J. *Adv. Funct. Mater.* **2014**, *24*, 6270.
- (58) Brédas, J.-L.; Calbert, J. P.; da Silva Filho, D. A.; Cornil, J. *Proc. Natl. Acad. Sci. U. S. A.* **2002**, *99*, 5804.
- (59) Da Silva Filho, D. A.; Kim, E. G.; Brédas, J.-L. *Adv. Mater.* **2005**, *17*, 1072.
- (60) Bagnis, D.; Beverina, L.; Huang, H.; Silvestri, F.; Yao, Y.; Yan, H.; Pagani, G. A.; Marks, T. J.; Facchetti, A. *J. Am. Chem. Soc.* **2010**, *132*, 4074.
- (61) Kasha, M. *Radiat. Res.* **1963**, *20*, 55.
- (62) Yamagata, H.; Maxwell, D. S.; Fan, J.; Kittilstved, K. R. A.; Briseno, L.; Barnes, M. D.; Spano, F. C. *J. Phys. Chem. C* **2014**, *118*, 28842.
- (63) Lin, J. D. A.; Mikhnenko, O. V.; Chen, J. R.; Masri, Z.; Ruseckas, A.; Mikhailovsky, A.; Raab, R. P.; Liu, J. H.; Blom, P. W. M.; Loi, M. A.; Garcia-Cervera, C. J.; Samuel, I. D. W.; Nguyen, T.-Q. *Mater. Horiz.* **2014**, *1*, 280.
- (64) Würthner, F.; Kaiser, T. E.; Saha-Möller, C. R. *Angew. Chem., Int. Ed.* **2011**, *50*, 3376.
- (65) Kurrle, D.; Pflaum, J. *Appl. Phys. Lett.* **2008**, *92*, 133306.
- (66) Hartnett, P. E.; Timalina, A.; Matte, H. S. S. R.; Zhou, N.; Guo, X.; Zhao, W.; Facchetti, A.; Chang, R. P. H.; Hersam, M. C.; Wasielewski, M. R.; Marks, T. J. *J. Am. Chem. Soc.* **2014**, *136*, 16345.